

Phase Composition and Superplastic Behavior of a Wrought AlCoCrCuFeNi High-Entropy Alloy

D.G. SHAYSULTANOV,¹ N.D. STEPANOV,¹ A.V. KUZNETSOV,¹
G.A. SALISHCHEV,¹ and O.N. SENKOV^{2,3}

1.—Laboratory of Bulk Nanostructured Materials, Belgorod State University, 85 Pobeda St., Belgorod 308015, Russia. 2.—UES, Inc., 4401 Dayton-Xenia Rd., Dayton, OH 45432, USA.
3.—e-mail: oleg.senkov.ctr@wpafb.af.mil

A cast AlCoCrCuFeNi high-entropy alloy was multiaxially forged at 950°C to produce a fine homogeneous mixture of grains/particles of four different phases with the average size of ~2.1 μm. The forged alloy exhibited unusual superplastic behavior accompanied by a pronounced softening stage, followed by a steady-state flow stage, during tensile deformation at temperatures of 800°C–1000°C and at strain rates of 10⁻⁴–10⁻¹ s⁻¹. Despite the softening stage, no noticeable strain localization was observed and a total elongation of up to 1240% was obtained. A detailed analysis of the phase composition and microstructure of the alloy before and after superplastic deformation was conducted, the strain rate and temperature dependences of the flow stress were determined at different stages of the superplastic deformation, and the relationships between the microstructure and properties were identified and discussed.

INTRODUCTION

High-entropy alloys (HEAs) are a relatively new class of metallic materials developed during recent decade.^{1–3} These alloys typically contain from 5 to 13 principal elements in approximately equimolar proportions.¹ The microstructure of these alloys is thought to consist preferably of disordered solid solutions, which are stabilized by a high entropy of mixing of the alloying elements.^{1,4–13} However, some HEAs also contain ordered solid-solution and/or intermetallic phases.^{14–16} For example, Cu-rich phases with B2 and/or L12 structure, an Al-Ni-rich phase with B2 structure, and a Fe-Cr-rich phase with a disordered face-centered cubic (fcc) structure can coexist in the AlCoCrCuFeNi alloy after casting.¹⁴

HEAs can offer some very attractive properties, such as high hardness and strength, high wear and creep resistance, high temperature stability, and low thermal conductivity, which make them desirable for different applications.^{1,17,18} Unfortunately, in many cases these alloys were studied in the as-cast condition, and very low room temperature ductility, or even brittle behavior, was often

reported. It is well known that thermomechanical treatment can refine the coarse dendritic microstructure formed during casting and can enhance the mechanical properties, especially ductility, of conventional metallic alloys. In a recent work,¹⁹ this approach was tried to improve the ductility of an AlCoCrCuFeNi HEA, which is inherently brittle in the as-cast condition. The alloy was hot worked by multiaxial forging to produce a fine-grained structure, which resulted in significantly improved ductility and strength at room temperature. Moreover, at high temperatures, the fine-grained alloy exhibited superplastic-like behavior.^{19,20} Enhanced ductility can open the way to the cost-effective production of complex parts from this new class of alloys. Unfortunately, the origins of the superplastic behavior of HEAs remain mostly unclear. In particular, contributions of different phases presented in the AlCoCrCuFeNi alloy in the superplastic behavior, as well as flow stress controlling mechanisms, have not yet been identified. In the current work, detailed phase and microstructure analyses of the fine-grained AlCoCrCuFeNi HEA have been conducted before and after superplastic deformation, a constitutive equation for the superplastic

flow has been determined, and the relationships between the microstructure and properties have been outlined and discussed.

EXPERIMENTAL PROCEDURES

An ingot of the AlCoCrCuFeNi alloy, at the equiatomic composition, was produced by induction melting of pure elements. The ingot was then electro-slag remelted and cast into a water-cooled copper mold. Melting and casting were conducted under high-purity argon atmosphere. The produced ingot was trimmed by cutting out about 10-mm-thick pieces from the top and bottom of the ingot, and a sample of 40 mm in diameter and 35 mm in length was machined from the remaining part of the ingot. The sample was homogenized at 960°C for 50 h and subjected to multidirectional forging at

950°C. Forging was performed using a DEVR 4000 hydraulic press (PLC Hydropress, Orenburg, Russia) equipped with an isothermal stamping tool. The ram speed was 1 mm/s and the total true strain achieved during forging was ~1000%.

Uniaxial tensile tests were conducted in air using an Instron 5882 testing machine (Instron Corporation, Norwood, MA, USA) equipped with a radiant furnace. Testing was performed at temperatures in the range of 800°C–1000°C and at strain rates in the range of 10^{-4} – 10^{-1} s⁻¹. Tensile specimens were heated to a testing temperature with a heating rate of ~15°C/min and equilibrated at the temperature for ~15 min. Gauge dimensions of the specimens were 16 × 3 × 1.5 mm³. The microstructures of polished cross-sections of the nondeformed and deformed specimens were studied using scanning electron microscopes (SEMs) Quanta 200 3D and

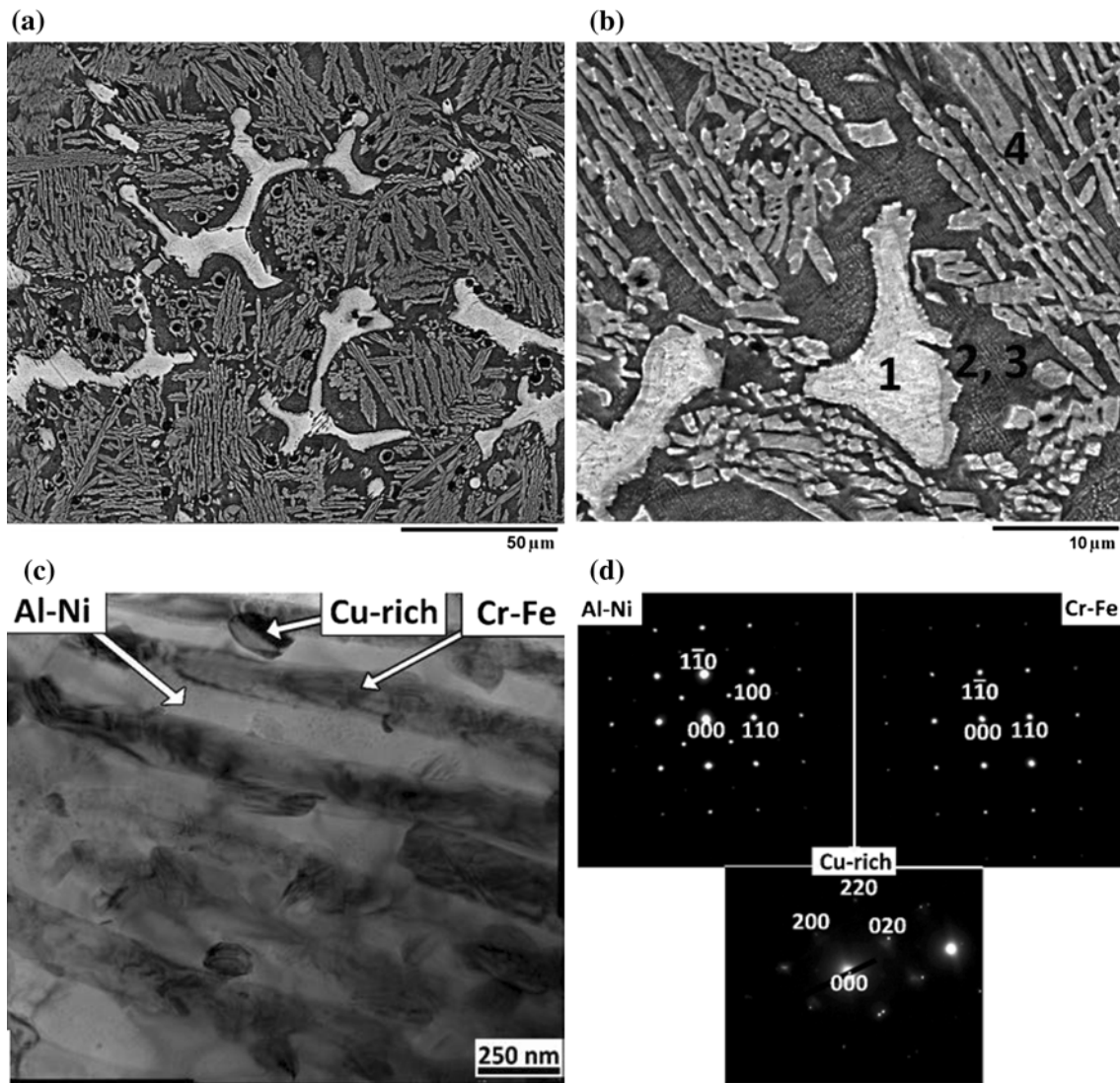


Fig. 1. Microstructure of the AlCoCrCuFeNi alloy in as-cast condition: (a, b) SEM backscattered electron images: (a) low magnification and (b) higher magnification with marked-up phases. The phase identifications and compositions are given in Table I. (c) TEM image of the modulated structure, which corresponds to the region identified by points 2 and 3 in (b). (d) Selected-area diffraction patterns from the phases shown in (c).

Quanta 600 (FEI Company, Hillsboro, OR, USA) equipped with backscattered electron detectors, energy-dispersive spectrometers (EDS), and electron backscattered diffraction (EBSD) detectors. Additional microstructural investigations were performed using transmission electron microscope (TEM) JEOL-2100 (JEOL Ltd., Tokyo, Japan) equipped with an EDS detector. A thorough phase analysis was conducted with the use of x-ray diffraction, SEM, EDS, EBSD, and TEM techniques. The average grain/particle size and the volume fractions of the phases and pores were determined using ASTM E112 and ASTM E562 standards. Thin TEM foils were prepared using an ion-beam polishing machine. Nanohardness testing was conducted using a Nano Indenter G200 (Agilent Technologies, Inc., Santa Clara, CA, USA) with Berkovich diamond pyramid.

RESULTS

Microstructure and Room-Temperature Properties

As-Cast Condition

In the as-cast condition, the AlCoCrCuFeNi alloy has a transformed dendritic structure (Fig. 1a) with the average dendrite cell size of about 50 μm . Interdendrite areas (bright ones, point 1 in Fig. 1b) are enriched with Cu and have, in accord with x-ray and electron diffraction analyses, an ordered (L1_2) fcc crystal structure (Table I).

The volume fraction of the Cu-rich phase is 12%. Dendrites have a complex structure, which was likely produced during solid-state reactions after the solidification. The base (dark) constituent of the dendrites has a modulated structure consisting predominantly of two Al-Ni-rich and Cr-Fe-rich, phases. These phases are indicated in Fig. 1b by points 2 and 3, respectively, and they are clearly seen in a TEM image (Fig. 1c) in the form of nanolamellae. The average lamellar thickness of the Al-Ni-rich phase is ~ 185 nm and that of Cr-Fe-rich phase is ~ 90 nm. Few ellipsoid-shaped Cu-rich nanoparticles, containing about 65% Cu, are also present inside the modulated structure. Selected-area electron diffraction patterns (SAEDPs) from these phases reveal an ordered B2 crystal structure of the Al-Ni-rich phase, a disordered bcc crystal structure of the Cr-Fe-rich phase, and a disordered fcc crystal structure of the Cu-rich nanoparticles (Fig. 1d). The volume fraction of the modulated structure is 43%. Coarse, mainly elongated, gray-colored particles are also found inside the dendrites (one of these particles is indicated by point 4 in Fig. 1b). They are enriched with Co, Cr, and Fe, have an ordered fcc (L1_2) crystal structure, and their volume fraction is 45%. The phase composition of the as-cast alloy is in a good agreement with previously reported data.¹⁴ The lattice parameters and chemical compositions of these phases are given

Table I. Crystal structure, phase composition, volume fraction, and properties of different phases in the as-cast AlCoCrCuFeNi alloy

Number	Phase ID	Crystal structure/lattice parameter (\AA)	Chemical composition (at.%)				Volume fraction (%)	Nanohardness (GPa)	Elastic modulus (GPa)
			Al	Cr	Fe	Ni			
1	Cu	fcc (L1_2)/3.629	13.5	2.5	4.6	12.5	61.9	12	3.78 \pm 0.50
2	Al-Ni	B2/2.876	27.4	4.0	12.6	19.4	28.1	8.6	158 \pm 6
3	Cr-Fe	bcc/2.876	1.0	50.6	29.1	15.4	2.0	43	206 \pm 21
4	Co-Cr-Fe	fcc (L1_2)/3.601	5.1	24.7	26.4	22.5	13.2	8.0	213 \pm 15

bcc base-centered cubic.

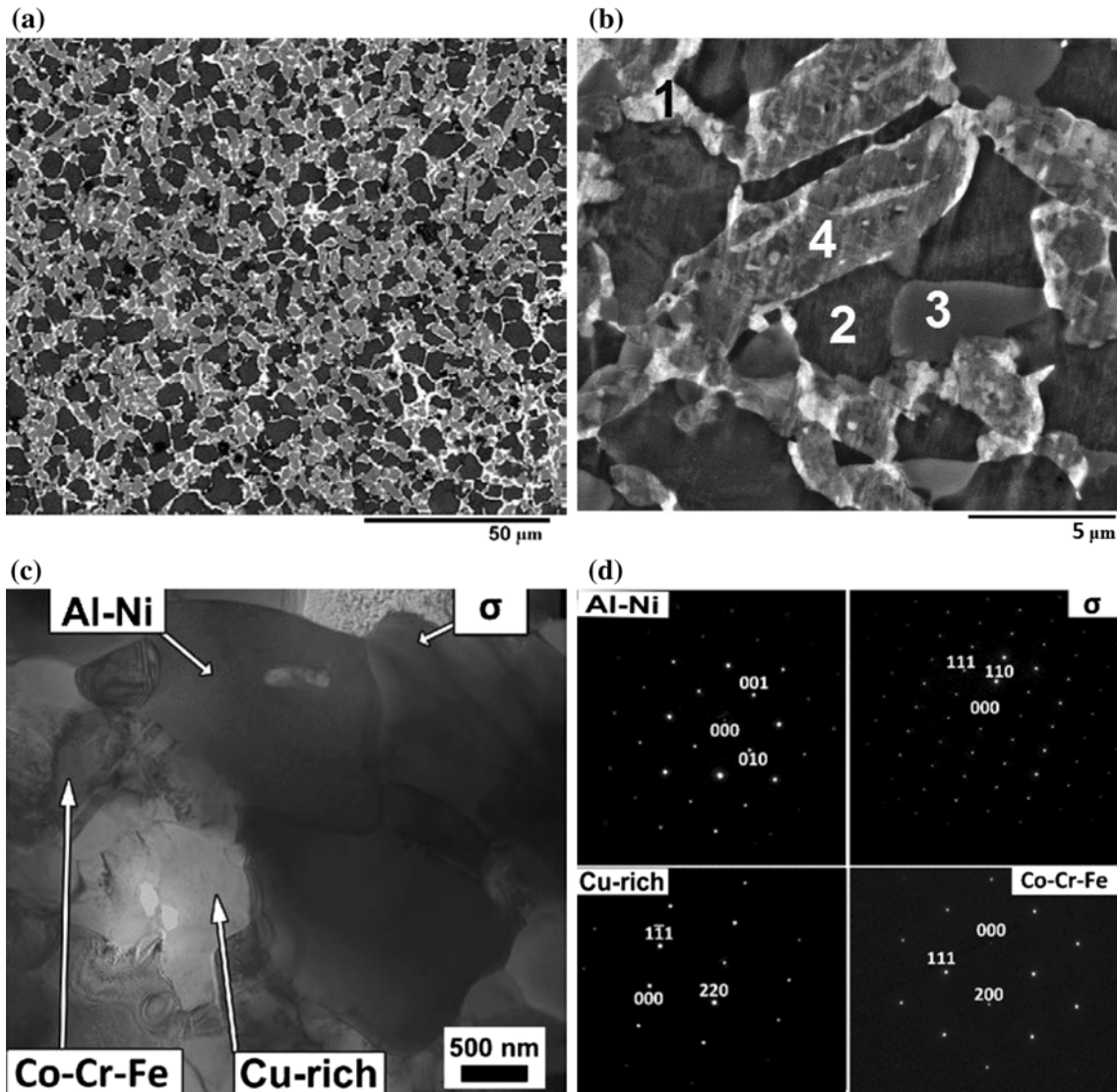


Fig. 2. Microstructure of the hot multiaxially forged AlCoCrCuFeNi alloy. (a, b) SEM backscattered electron images: (a) low magnification and (b) higher magnification with marked-up phases. The phase identifications and compositions are given in Table II. (c) TEM image of a region containing four phases. (d) Selected-area diffraction patterns from the phases indicated in (c).

in Table I. Nanohardness measurements showed distinctively different behavior of the individual phases (Table I). The Cu-rich phase is the softest and its hardness is ~ 3.8 GPa. The modulated structure consisting of fine lamellas of the Al-Ni-rich and Cr-Fe-rich phases has the highest hardness of ~ 7.2 GPa. (It was not possible to measure nanohardness of these two phases separately because of their fine scale.) The Co-Cr-Fe-rich phase has an intermediate hardness of ~ 5.5 GPa. The elastic moduli of the alloy constituents are 158 GPa for the Cu-rich phase, 206 GPa for the modulated structure, and 213 GPa for the Co-Cr-Fe-rich phase.

Hot-Forged Condition

After hot isothermal forging, the AlCoCrCuFeNi alloy has a rather homogeneous mixture of fine

particles of four different phases, with the average grain/particle size of about $2.1 \mu\text{m}$ (Fig. 2a). The chemical compositions, crystal structure, and lattice parameters of these phases are given in Table II.

The fcc crystal structures of the Cu-rich (#1 in Fig. 2b and Table II) and Co-Cr-Fe-rich (#4) phases, which were ordered in the as-cast condition, become disordered after hot forging. The lattice parameter of the Cu-rich phase slightly increases, while that of the Co-Cr-Fe-rich phase slightly decreases, probably due to modified compositions of these phases after the forging. The composition and the B2 crystal structure of the Al-Ni-rich phase (#2) were not affected by hot working. However, a disordered bcc crystal structure of the Cr-Fe-rich phase in the as-cast condition transforms, after forging, to an ordered σ phase, with a tetragonal crystal structure. These x-ray diffraction results are supported by a

Table II. Crystal structure, phase composition, volume fraction, and properties of different phases in the hot-forged AlCoCrCuFeNi alloy

Number	Phase ID	Crystal structure/lattice parameter (Å)	Chemical composition (at.%)				Volume fraction (%)	Nanohardness (GPa)	Elastic modulus (GPa)		
			Al	Cr	Fe	Ni					
1	Cu	FCC/3.634	11.2	2.0	3.0	8.4	72.0	3.03 ± 0.40	162 ± 5		
2	Al-Ni	BCC (B2)/2.877	32.6	4.7	10.4	15.3	26.1	6.84 ± 0.21	190 ± 18		
3	σ	Tetragonal ($D8_b/a = 8.810$) $b = 4.560$	2.9	46.7	23.9	19.0	4.8	9.87 ± 1.41	233 ± 25		
4	Co-Cr-Fe	FCC/3.598	5.3	24.4	28.1	22.6	11.6	7.9	30	4.15 ± 0.05	205 ± 5

thorough TEM analysis. For example, Fig. 2d illustrates SAEDPs taken from the phases indicated on the TEM image in Fig. 2c. The presence of super-lattice reflections reveals ordering of Al-Ni-rich and σ phases. The super-lattice reflections are, however, absent on the SAEDPs from the Cu-rich and Co-Cr-Fe-rich phases confirming their disordered state. Relative to the as-cast condition, the volume fraction of the Cu-rich phase increases from 12% to 17%, while the volume fraction of the Co-Cr-Fe-rich phase decreases from 45% to 30%. The volume fractions of the Al-Ni-rich and σ phases are 46% and 7%, respectively. The grains or particles of the Al-Ni-rich, Co-Cr-Fe-rich, and σ phases have nearly equiaxed shape. However, the Cu-rich phase is smeared and mainly located at the interface boundaries between the other three phases (Fig. 2b).

Hot forging softens the Cu-rich and Co-Cr-Fe-rich phases and their nanohardness decreases to 3.0 GPa and 4.2 GPa, respectively (Table II). The σ phase has the highest hardness of ~9.9 GPa. These values are in a good agreement with the data available in the literature for Cu, up to 2.2 GPa,²¹ and for the σ phase, up to 17 GPa,²² taking into account the difference in chemical composition. The nanohardness of the Al-Ni-rich B2 phase is 6.8 GPa. The elastic modulus of the Cu-rich phase remains almost unaffected by the hot forging and is 162 GPa. The elastic moduli of the Al-Ni and σ phases are 190 GPa and 233 GPa, respectively, and the modulus of the Co-Cr-Fe-rich phase is 205 GPa.

Superplasticity of the Hot-Forged Alloy

Deformation Behavior

The tensile stress-strain curves obtained during testing at temperatures of 800°C, 900°C, and 1000°C and different strain rates are shown on Fig. 3. The values of the yield strength $\sigma_{0.2}$, ultimate tensile strength (peak strength) σ_u , steady-state flow stress σ_{ss} , and elongation to fracture δ are summarized in Table III.

The deformation behavior noticeably depends on the strain rate. During deformation at $T = 800^\circ\text{C}$ and 900°C and at a strain rate of $\dot{\epsilon} = 10^{-2} \text{ s}^{-1}$, the flow stress reaches a peak value and then drops rapidly until the fracture occurs. With a decrease in the strain rate and an increase in temperature, the flow stress peak becomes less pronounced and the softening stage, followed after the peak overshoot, gradually transforms to a prolonged steady-state flow stage. The steady-state flow stress σ_{ss} can be three to eight times smaller than the peak stress σ_u . For example, at $T = 1000^\circ\text{C}$ and $\dot{\epsilon} = 10^{-1} \text{ s}^{-1}$, $\sigma_u = 55 \text{ MPa}$ and $\sigma_{ss} = 7 \text{ MPa}$, respectively. Both $\sigma_{0.2}$ and σ_u show an order of magnitude decrease in their values when $\dot{\epsilon}$ decreases by the two orders of magnitude, at all studied temperatures. For example, at $T = 1000^\circ\text{C}$ and $\dot{\epsilon} = 10^{-1} \text{ s}^{-1}$, $\sigma_u = 54.8 \text{ MPa}$, while at $\dot{\epsilon} = 10^{-3} \text{ s}^{-1}$, $\sigma_u = 5.1 \text{ MPa}$. The dependence

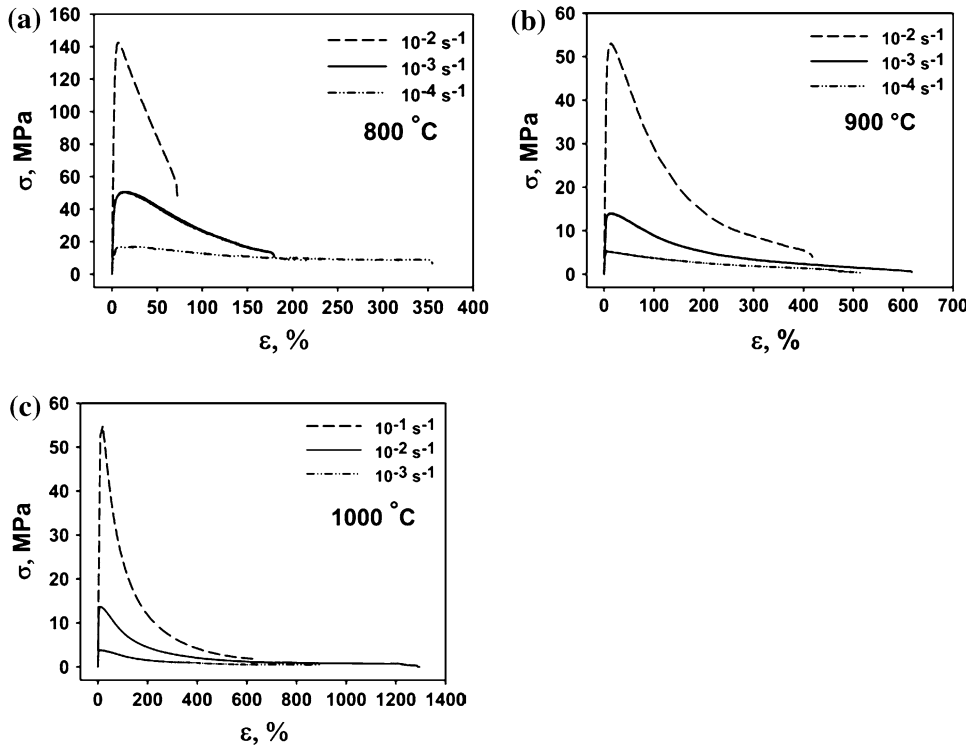


Fig. 3. Tensile stress–strain curves of the hot-forged AlCoCrCuFeNi alloy samples at different temperatures and strain rates: (a) $T = 800^\circ\text{C}$, (b) $T = 900^\circ\text{C}$, and (c) $T = 1000^\circ\text{C}$.

Table III. Tensile properties of the hot-forged AlCoCrCuFeNi alloy

T ($^\circ\text{C}$)	800			900			1000			
	$\dot{\epsilon}$ (s^{-1})	10^{-4}	10^{-3}	10^{-2}	10^{-4}	10^{-3}	10^{-2}	10^{-3}	10^{-2}	
$\sigma_{0.2}$ (MPa)		8	35	105	4	12	42	3	12	42
σ_u (MPa)		17	51	142	5	14	53	5	14	55
σ_{ss} (MPa)		8.6	—	—	1.8	3.5	9.0	1.2	3.0	7.0
δ (%)		325	160	60	490	585	350	850	1240	600



Fig. 4. Photographs of tensile specimens of the hot-forged AlCoCrCuFeNi alloy after superplastic deformation at $T = 1000^\circ\text{C}$ and different strain rates.

of the total elongation to fracture δ on the strain rate demonstrates a pronounced maximum at a certain strain rate. During tensile testing at $T = 800^\circ\text{C}$, the maximum value of $\delta = 325\%$ is

achieved at $\dot{\epsilon} = 10^{-4}\text{ s}^{-1}$. With an increase in T , δ increases and the peak ductility is observed at higher $\dot{\epsilon}$ values. For example, at $T = 900^\circ\text{C}$, δ has a maximum value of 585% at $\dot{\epsilon} = 10^{-3}\text{ s}^{-1}$, while at $T = 1000^\circ\text{C}$, the peak elongation of 1240% is observed at $\dot{\epsilon} = 10^{-2}\text{ s}^{-1}$. The results also show that the flow stress substantially decreases as the testing temperature increases. For example, at $\dot{\epsilon} = 10^{-3}\text{ s}^{-1}$, σ_u decreases from 51 MPa to 5 MPa with an increase in T from 800°C to 1000°C . An inspection of the tensile tested specimens (Fig. 4) shows rather homogeneous plastic deformation, with very little evidence of the strain localization in spite of a very pronounced softening stage.

Constitutive Equation and Activation Analysis

During high-temperature deformation, the relationship of the flow stress on strain rate and

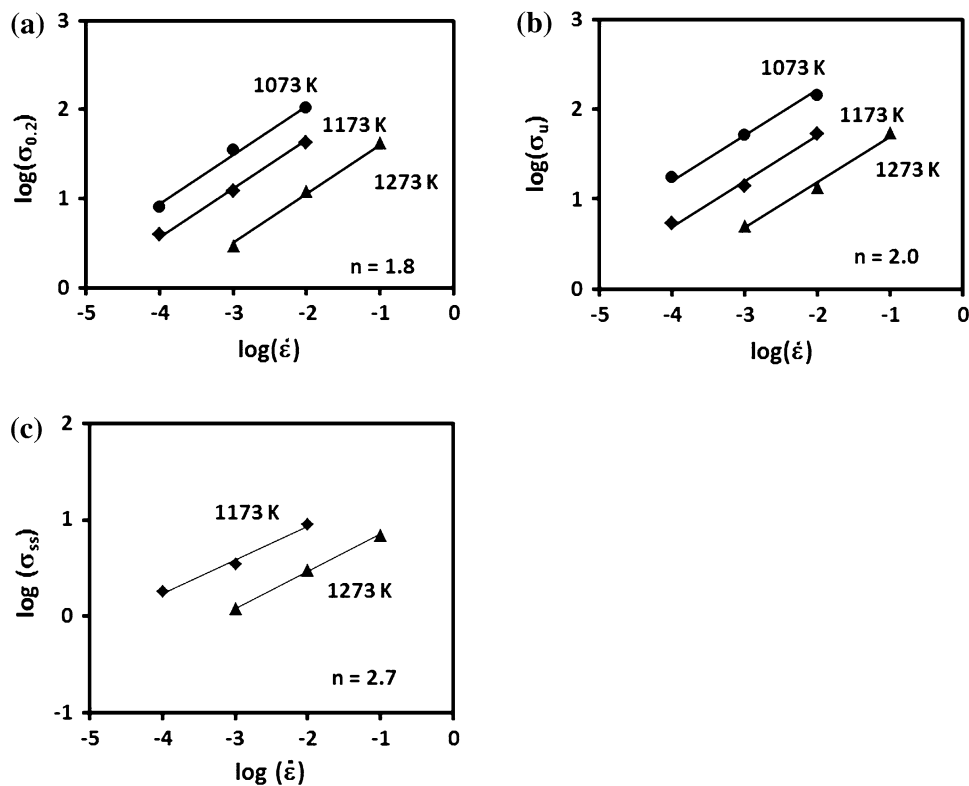


Fig. 5. Logarithmic dependences of (a) the yield stress $\sigma_{0.2}$, (b) peak stress σ_u , and (c) steady-state flow stress σ_{ss} on the strain rate $\dot{\varepsilon}$ at $T = 1073$ K (800°C), 1173 K (900°C), and 1273 K (1000°C).

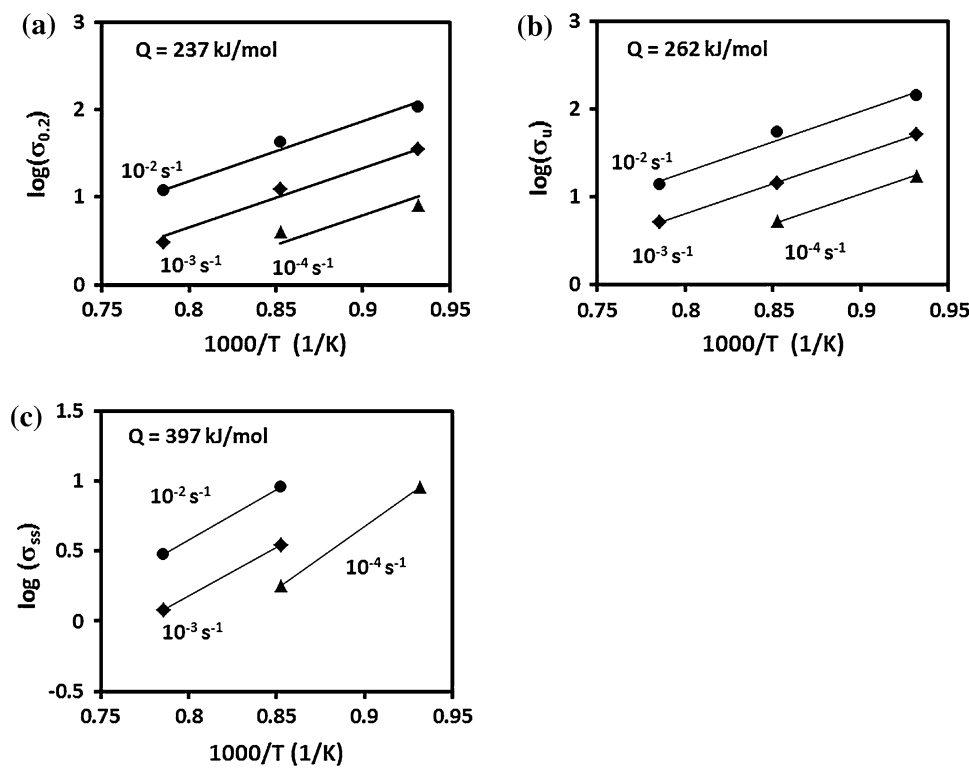


Fig. 6. Dependences of (a) $\log\sigma_{0.2}$, (b) $\log\sigma_u$, and (c) $\log\sigma_{ss}$ on the inverse absolute temperature at $\dot{\varepsilon} = 10^{-4} \text{ s}^{-1}$, 10^{-3} s^{-1} , and 10^{-2} s^{-1} .

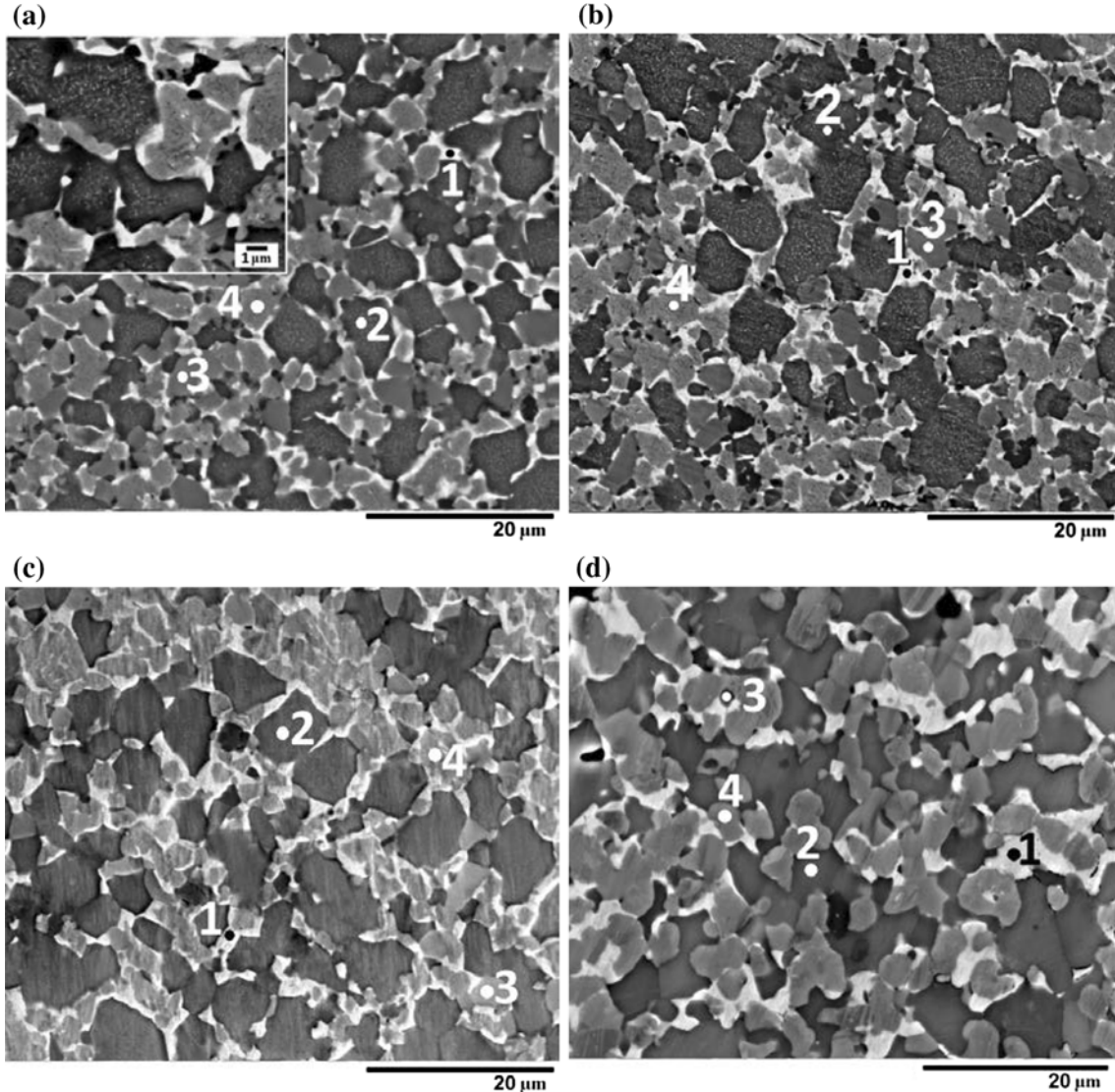


Fig. 7. Microstructure of the hot-forged AlCoCrCuFeNi alloy specimens after tensile testing at (a, b) $T = 800^\circ\text{C}$ and $\dot{\varepsilon} = 10^{-2} \text{ s}^{-1}$; (c, d) $T = 1000^\circ\text{C}$ and $\dot{\varepsilon} = 10^{-2} \text{ s}^{-1}$. (a, c) Nondeformed (head) regions and (b, d) deformed regions. Phase IDs and compositions are given in Table V.

temperature is generally described with the use of a Zener–Hollomon parameter $Z(\sigma)$:^{23–25}

$$Z(\sigma) = A\sigma^n = \dot{\varepsilon}\exp(Q/RT), \quad (1)$$

where Q is the activation energy, n is the stress exponent, A is a constant sensitive to the deformation mechanism, and R is the gas constant. The parameters n and Q can be determined with the use of the following relations:

$$n = \left. \frac{\partial \ln \dot{\varepsilon}}{\partial \ln \sigma} \right|_T \quad (2)$$

$$Q = -R \left. \frac{\partial \ln \dot{\varepsilon}}{\partial (1/T)} \right|_\sigma \equiv nR \left. \frac{\partial \ln \sigma}{\partial (1/T)} \right|_{\dot{\varepsilon}}. \quad (3)$$

Figure 5 shows linear dependences of $\log(\sigma_{0.2})$, $\log(\sigma_u)$, and $\log(\sigma_{ss})$ on $\log(\dot{\varepsilon})$ at three different temperatures, 1073 K, 1173 K, and 1273 K. The slopes of these curves (n) do not depend on temperature; however, they seem to be different at different stages of the plastic deformation. For example, at the beginning of plastic deformation, $n_{0.2} = 1.8$. When deformation progresses and the flow stress approaches its peak value, n slightly increases to $n_p = 2.0$. When the steady-state flow condition is achieved, n increases to $n_{ss} = 2.7$.

Figure 6 shows the linear dependences of $\log(\sigma_{0.2})$, $\log(\sigma_u)$, and $\log(\sigma_{ss})$ on the inverse absolute temperature, $1/T$, obtained at three different strain rates. The slopes of these dependences determine the activation energies, in accordance with Eq. 3. A

Table IV. Average size d_{av} of grain/particles in deformed and undeformed parts of specimens after tensile testing at different temperatures and strain rates

T (°C)	800			900			1000			
	$\dot{\varepsilon}$ (s^{-1})	10^{-4}	10^{-3}	10^{-2}	10^{-4}	10^{-3}	10^{-2}	10^{-3}	10^{-2}	
d_{av} (μm) deformed region		1.7 ± 1.5	1.5 ± 1.4	2.0 ± 1.4	1.7 ± 1.2	2.4 ± 1.9	1.9 ± 1.5	1.8 ± 1.2	2.0 ± 1.4	2.2 ± 1.7
d_{av} (μm) nondeformed region		1.9 ± 1.4	1.9 ± 1.5	1.8 ± 1.2	1.8 ± 1.3	1.9 ± 1.3	1.9 ± 1.3	2.0 ± 1.6	2.0 ± 1.4	2.1 ± 1.4

Table V. Chemical composition and volume fraction of different phases in the hot forged AlCoCrCuFeNi alloy after tensile testing at different temperatures and strain rates

Number	Phase ID	Chemical composition (at.%)						Volume fraction (%)
		Al	Cr	Fe	Co	Ni	Cu	
$T = 800^\circ\text{C}; \dot{\varepsilon} = 10^{-2} \text{ s}^{-1}$; nondeformed region								
1	Cu	10.6	2.1	3.3	3.8	7.6	72.6	17
2	Al-Ni	26.3	7.3	12.6	15.8	26.0	12.0	44
3	σ	2.7	49.5	23.7	18.1	4.7	1.4	5
4	Co-Cr-Fe	7.5	23.0	27.1	22.2	12.3	8.0	34
$T = 800^\circ\text{C}; \dot{\varepsilon} = 10^{-2} \text{ s}^{-1}$; deformed region								
1	Cu	9.6	1.6	2.7	3.2	7.0	75.7	17
2	Al-Ni	29.2	5.5	11.8	16.9	28.4	8.1	41
3	σ	2.9	50.2	23.33	17.9	4.4	1.3	5
4	Co-Cr-Fe	6.8	23.5	28.7	22.5	12.0	6.5	37
$T = 1000^\circ\text{C}; \dot{\varepsilon} = 10^{-2} \text{ s}^{-1}$; nondeformed region								
1	Cu	12.2	2.0	3.9	4.4	10.4	67.1	17
2	Al-Ni	26.4	6.9	12.1	15.6	24.8	14.3	49
3	σ	2.5	49.6	24.3	17.8	4.5	1.3	3
4	Co-Cr-Fe	6.9	24.0	28.4	22.1	11.8	6.8	31
$T = 1000^\circ\text{C}; \dot{\varepsilon} = 10^{-2} \text{ s}^{-1}$; deformed region								
1	Cu	14.7	2.2	4.0	4.0	10.2	64.8	15
2	Al-Ni	29.8	6.40	11.2	19.1	24.6	13.0	43
3	Cr	2.9	71.8	10.0	6.1	4.3	5.0	2
4	Co-Cr-Fe	8.0	24.6	27.0	22.0	12.2	6.2	30

dramatic increase in the activation energy was found during the transition from the beginning stages of the plastic deformation to the steady-state flow behavior. For example, $Q_{0.2} = 237 \text{ kJ/mol}$ at the plastic yielding and $Q_p = 262 \text{ kJ/mol}$ when the peak stress is achieved. However, at plastic strains of 200% and above, when the steady-state flow occurs, the activation energy increases to $Q_{ss} = 394 \text{ kJ/mol}$.

Using the experimentally determined parameters n and Q , the parameter A in Eq. 1 was determined at the three stages of plastic deformation: $A_{0.2} = 5.57 \times 10^5 \text{ s}^{-1} \text{ MPa}^{-n}$, $A_p = 2.13 \times 10^6 \text{ s}^{-1} \text{ MPa}^{-n}$, and $A_{ss} = 7.73 \times 10^{12} \text{ s}^{-1} \text{ MPa}^{-n}$.

Microstructure and Phase Evolution

The microstructure studies did not reveal significant changes in the average grain/particle size (Fig. 7; Table IV) after tensile testing. It remained nearly constant, about 2 μm , both in deformed and

undeformed sections of the tensile tested samples and it was insensitive to the tensile testing parameters.

The chemical compositions of the Cu-rich, Al-Ni-rich, and Co-Cr-Fe-rich phases of the hot-forged Al-CoCrCuFeNi alloy did not change significantly after tensile testing (Table V). Only the concentration of Cu in the Cu-rich phase in the deformed sections of the specimens noticeable varied; e.g., after the tensile testing at 800°C it increased to 76%, and after testing at 1000°C it decreased to 65%, relative to 72% in the forged condition, before tensile testing. Additionally, fine precipitates form inside the Al-Ni-rich phase after testing at $T = 800^\circ\text{C}$ (shown in a higher magnification insert of Fig. 7a). These precipitates are composed mainly of Cu. They are found both in deformed and nondeformed regions of the tensile specimens. After testing at higher temperatures, no signs of these precipitates were found. It should be noted that the formation of similar fine Cu-rich precipitations inside other phases was previously reported for

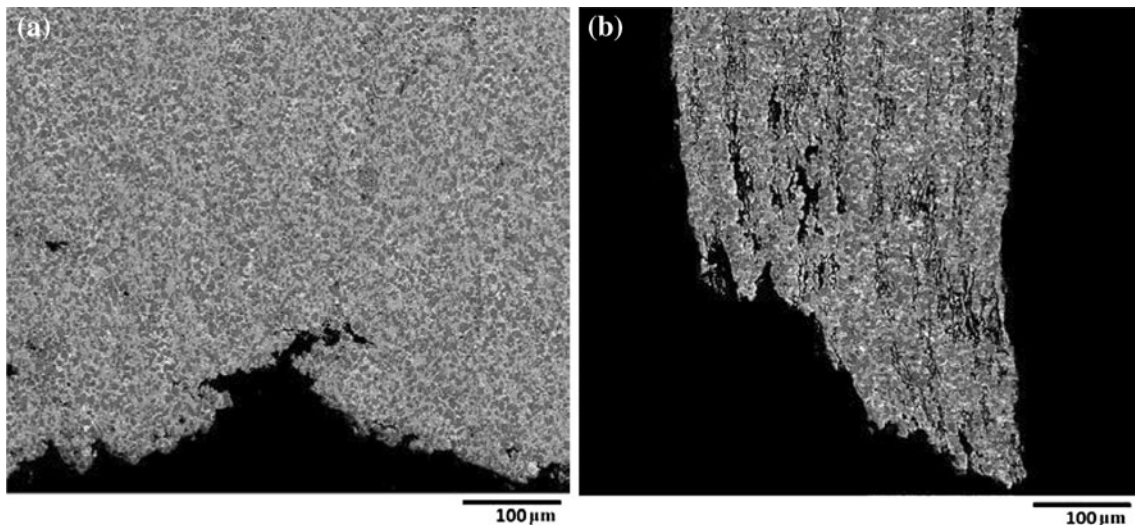


Fig. 8. Porosity developed in the hot multiaxially forged AlCoCrCuFeNi alloy after tensile testing at (a) $T = 800^\circ\text{C}$ and (b) $T = 1000^\circ\text{C}$. $\dot{\varepsilon} = 10^{-2} \text{ s}^{-1}$.

Table VI. Volume fraction of pores after tensile testing at different temperatures and strain rates

T ($^\circ\text{C}$)	800			900			1000		
	10^{-4}	10^{-3}	10^{-2}	10^{-4}	10^{-3}	10^{-2}	10^{-3}	10^{-2}	10^{-1}
$\dot{\varepsilon}$ (s^{-1})									
Volume fraction of pores (%)	0.3	3.9	9.7	1.1	3.3	11.5	13.1	8.0	5.8
Volume fraction of pores per 1% strain (% $\times 10^{-3}$)	0.9	24.9	161.7	2.3	5.6	32.9	15.4	6.5	9.7

the FeCoNiCrCu_{0.5} alloy after annealing at the temperature of 950°C .²⁶ As the content of Cu in the studied alloy is higher, it might be hypothesized that Cu-rich precipitates appear at lower temperatures. The volume fractions of the Cu-rich, Al-Ni-rich, and Co-Cr-Fe-rich phases remained nearly unchanged in the nondeformed sections of the tensile samples. In the deformed section, after testing at 1000°C , the volume fraction of the Al-Ni-rich phase decreased to 41%–43%, and the volume fraction of the Co-Cr-Fe-rich phase increased to 30%–37%. The volume fraction of the Cu-rich phase remained almost unchanged and was ~15%–17%. The σ phase was not detected in the deformed section of the samples after tensile testing at 1000°C (Fig. 7d; Table V). Instead, a fine Cr-rich phase, containing about 70%–80% Cr, was present (point 3 in Fig. 7d). It is interesting to note that the σ phase retained in the nondeformed sections of these samples (Fig. 7a, c; Table V), although its volume fraction slightly decreased, to 3%–5%. This phase was also present after testing at lower temperatures, e.g., at $T = 800^\circ\text{C}$ (Fig. 7b; Table V).

Tension testing resulted in the development of porosity inside deformed regions (Fig. 8a, b; Table VI).

The volume fraction of pores in specimens tested at $T = 800^\circ\text{C}$ and 900°C increased rapidly with an increase in strain rate. For instance, the volume fraction of pores was 0.3% at $T = 800^\circ\text{C}$ and $\dot{\varepsilon} = 10^{-4} \text{ s}^{-1}$, while it was 9.7% at $T = 800^\circ\text{C}$ and

$\dot{\varepsilon} = 10^{-2} \text{ s}^{-1}$. On the other hand, the volume fraction of pores in specimens tested at $T = 1000^\circ\text{C}$ had the tendency to decrease from 13.1% to 5.8% with an increase in $\dot{\varepsilon}$ from 10^{-3} s^{-1} to 10^{-1} s^{-1} . It is necessary to point out that at the same strain rate and temperature conditions, the volume fraction of the pores increases with plastic strain.²⁷ Therefore, the specimens, which showed higher elongation (Table III), may have a higher volume fraction of pores. To identify the real effect of the temperature and strain rate on the porosity formation, the average rate of the pore volume fraction development per 1% elongation f_p was calculated (Table VI). It can be seen that the rate of the pore accumulation is minimum $f_p = 9 \times 10^{-4} \text{ %}/\%$, during deformation at $T = 800^\circ\text{C}$ and $\dot{\varepsilon} = 10^{-4} \text{ s}^{-1}$. At 800°C , it rapidly increases to $f_p = 0.16 \text{ %}/\%$ with an increase in $\dot{\varepsilon}$ to 10^{-2} s^{-1} . At $T = 900^\circ\text{C}$, f_p increases from 2.3×10^{-3} to 3.3×10^{-2} with an increase in $\dot{\varepsilon}$ from 10^{-4} s^{-1} to 10^{-2} s^{-1} . At $T = 1000^\circ\text{C}$, f_p decreases from 1.5×10^{-2} to 6.5×10^{-3} with an increase in $\dot{\varepsilon}$ from 10^{-3} s^{-1} – 10^{-2} s^{-1} , and then f_p increases to 9.7×10^{-3} with a further increase in $\dot{\varepsilon}$ to 10^{-1} s^{-1} .

DISCUSSION

Thermomechanical treatment by hot multiaxial forging of the as-cast AlCoCrCuFeNi HEA resulted

in the formation of a fine-grained multiphase structure with the average grain/particle size of $\sim 2.1 \mu\text{m}$. This fine-grained structure was likely produced by fragmentation, dynamic recrystallization, spheroidization, and a mixture of severely deformed phases. The hot forging also considerably modified the phase composition. First, the Cu-rich phase became disordered, the amount of Cu in this phase increased from $\sim 62\%$ to 72% , and the phase volume fraction increased from $\sim 12\%$ to 17% . A lack of the necessary amount of the alloying elements can prevent ordering.²⁸ Second, the bcc Cr-Fe-rich phase disappeared, the ordered (L1₂) Co-Cr-Fe phase became disordered and its volume fraction decreased from 45% to $\sim 30\%$, and a new tetragonal σ phase, at the volume fraction of $\sim 7\%$, was detected. Third, the ordered (B2) Al-Ni-rich phase became the major phase at the volume fraction of 46% . Commonly in steels, the σ phase is formed from the ferrite (bcc) phase at $T \leq 800^\circ\text{C}$ to 900°C ,²⁹ so it may be hypothesized that similar process occurred in the studied alloy during or after the hot forging and the σ phase formed from the bcc Cr-Fe-rich phase. It should be noted that the phase transformations in the HEAs still remain largely unclear, especially those that are related to thermomechanical treatment. This topic requires further, more detailed research.

The nanohardness and elastic modulus measurements revealed that the individual phases in the forged alloy had distinctively different deformation characteristics at room temperature. Nanohardness of the softest phase (Cu-rich) is more than three times lower than that of the hardest one (σ phase). It should be noted that a different mechanical behavior of different structural constituents was also reported for the Al_{0.8}CoCrCuFeNi alloy by Liu et al.³⁰ The strength of material is generally proportional to the shear modulus,²³ so that a phase with the higher elastic modulus is generally stronger. It is therefore thought that, at room temperature, Cu-rich phase is the softest one, followed by the Co-Cr-Fe-rich and Al-Ni-rich phases, while the σ phase is the strongest phase.

The relative properties of the phases can however change noticeably with temperature, as the strength of a phase having a lower melting temperature decreases more rapidly with an increase in temperature than the strength of a phase with a higher melting temperature. One can therefore expect that the Cu-rich phase, for which the melting temperature is about 1100°C ,²⁸ is the softest phase at $T = 800^\circ\text{C}$ to 1000°C . The fcc Co-Cr-Fe-rich phase has a significantly higher melting temperature, over 1400°C ,³¹ but it is known that austenitic high-Cr stainless steels tend to significantly soften at $T \geq 800^\circ\text{C}$.³² It is therefore suggested that the Co-Cr-Fe-rich phase would be the second softest phase at $T = 800^\circ\text{C}$ to 1000°C . The binary AlNi (B2) phase melts in the range of 1400°C to 1638°C , depending on its stoichiometry, and may retain high strength

up to 1200°C .³³ However, the melting temperature and thermal stability of the Al-Ni-rich phase, which is present in the AlCoCrCuFeNi alloy and is heavily alloyed with other elements, is not known and thus one can only speculate that the high-temperature strength of this phase is higher than that of Cu-rich and Co-Cr-Fe-rich phases. The σ phase is unstable at $T \geq 800^\circ\text{C}$ to 900°C ,²⁹ therefore, no contribution to the strength from this phase is expected at the tensile testing temperatures.

The multiphase structure, together with a significant difference in the mechanical properties of the individual phases, generally makes it difficult to maintain strain compatibility between the particles of different phases during tensile testing. Maintaining strain compatibility is necessary for preventing void and crack formation at the interfaces and thus obtaining high ductility. Surprisingly, the wrought AlCoCrCuFeNi alloy with the fine, multiphase structure reveals very high values of elongation to fracture and superplastic behavior (Table III). The strain rate sensitivity parameter $m = 1/n$ is in the range of 0.37 – 0.56 , which is consistent with $m = 0.5$ and is usually associated with fine-grained superplasticity, when grain boundary sliding (GBS) is the main deformation mechanism.²⁷ (For the multiphase structures consisting of the mixture of fine particles of different phases, the term GBS is also used to describe sliding along the interface boundaries.) At the same time, the observed stress-strain curves with a very pronounced peak followed by a softening stage, at which the flow stress decreases by three to eight times, depending on the loading conditions (Fig. 3), are quite unusual for the superplastic behavior. Indeed, the peak overshoot and the strain-induced softening are generally not observed during superplastic deformation, as they result in extensive neck formation and strain localization, leading to rapid failure.^{23,27,34} Remarkably, the considerable decrease in the flow stress occurring during accumulation of $\sim 200\%$ of the tensile strain did not produce any noticeable necking in the AlCoCrCuFeNi alloy samples. Instead, a rather homogeneous plastic flow occurred and the softening stage gradually transformed to the steady-state flow stage (Figs. 3, 4).

The presence of the stress peak overshoot can be anticipated if structural and/or phase transformations accompany the plastic deformation. For example, the activation of dynamic recrystallization refines the microstructure and can considerably reduce the plastic flow stress.²⁴ Dynamic recrystallization can also provide a source for accommodation of GBS and can promote superplastic behavior.³⁵ However, no grain refinement occurred in the Al-CoCrCuFeNi alloy during the high-temperature deformation (Table IV). The forged microstructure of this alloy was highly stable and no grain/particle refinement or coarsening was observed after annealing at 1000°C for about 25 h (this condition corresponds to the nondeformed section of a

specimen tested at $\dot{\varepsilon} = 10^{-3}$ s⁻¹). The absence of grain growth and grain refinement during the high-temperature tensile testing can be related to the complexity of the microstructure of the alloy. Evidently, mass transfer by diffusion is required for growth of particles of different phases. However, as the microstructure of the alloy is a complex mixture of the phases with different compositions and properties, the mass transfer is difficult.⁴⁶

There are few indications that the phase transformations have occurred during the tensile testing. These are (i) noticeable changes in the chemical composition of the Cu-rich phase, (ii) formation of fine precipitates enriched with Cu inside the Al-Ni-rich phase, (iii) a decrease in the volume fraction of the Al-Ni-rich phase from 46% to 41%–43%, (iv) an increase in the volume fraction of the Co-Cr-Fe-rich phase from 30% to 37%–40%, and (v) disappearance of the σ phase and formation of the Cr-rich phase. Unfortunately, the phase diagram has not yet been developed for the studied AlCoCrCuFeNi alloy, and thus, it is not known what phases are present at the testing temperatures. The fact that the average grain/particle size of the phases does not change after the testing may suggest that the phase transformations occur within each individual particle, and they do not involve considerable composition changes. For example, transformation of the ordered B2 Al-Ni-rich phase into a disordered bcc solid-solution phase at temperatures above 850°C has recently been reported for an Al_{0.5}CoCrCuFeNi HEA.³⁶ Thermodynamic modeling of the phase diagrams of similar HEA systems, Al_xCoCrFeNi³⁷ and Al_{0.5}CoCrCuFeNi,³⁶ predicts that the hard-to-deform and brittle σ phase is thermodynamically unstable at $T \geq 800^\circ\text{C}$. Comparing the chemical compositions of the phases before and after the high-temperature deformation (Tables 2, 5) suggests that the σ phase decomposes into softer and more ductile Cr-rich and Co-Cr-Fe-rich phases.

Due to sluggish diffusion in HEAs,⁴⁶ the transformation of the phases, presented at room temperature, into high-temperature phases, which are in thermodynamic equilibrium at the temperatures of tensile testing, can be very much delayed. Plastic deformation, however, can accelerate this transformation by producing lattice defects, such as dislocations and excess vacancies. It is likely that the critical plastic strain is required to initiate the phase transformations, and it corresponds to the peak strength on the deformation curves. A rapid decrease in the flow stress after the peak overshoot is thus due to the transformation of stronger lower temperature phases into softer high-temperature phases. To avoid strain localization, however, this process must occur simultaneously in the whole working region of a tension tested specimen.

In addition to being the sources of the alloy softening, the phase transformations occurring during the tensile testing can effectively accommodate GBS.²⁷ These transformations are controlled by the

lattice diffusion of the alloying elements, and thus, the activation energy of the plastic flow should correspond to the activation energy of the diffusion in a phase that accommodates the GBS. The thermal activation analysis of the superplastic deformation of the AlCoCrCuFeNi HEA shows different activation energies at different stages of the plastic flow: in particular, at the plastic yielding ($\varepsilon = 0.2\%$), $Q_{0.2} = 236$ kJ/mol; when the peak stress approaches, $Q_p = 262$ kJ/mol; and at the steady-state flow stage $Q_{ss} = 394$ kJ/mol. These experimental values of the activation energies can be compared with the self-diffusion activation energy of Cu (211 kJ/mol),³⁸ diffusion of Co in pure Cu (231 kJ/mol)³⁹ self-diffusion activation energy of Fe in γ -Fe and stainless steels (270 kJ/mol–312 kJ/mol),^{40,41} activation energy of self-diffusion and creep of Ni (284 kJ/mol \pm 12 kJ/mol),^{42,43} self-diffusion activation energy of Cr (339 \pm 12 kJ/mol),⁴⁴ and activation energy of creep of Ni-based alloys (390–500) kJ/mol.^{43,45} Using this comparison and taking into account that the rates of diffusion in the HEAs are slower than in pure metals,⁴⁶ one can suggest that the superplastic deformation of the AlCoCrCuFeNi HEA is realized through the GBS accommodated by the following activation processes: (i) at the beginning of deformation by the plastic deformation in the Cu-rich phase; (ii) in the vicinity of the peak stress and at the softening stage by the Fe- and/or Ni-diffusion-controlled transformations and plastic deformation in the Co-Cr-Fe-rich and/or Al-Ni-rich phases; and (iii) during the steady-state plastic flow by the plastic deformation of equilibrium high-temperature phases, controlled by complex diffusion with a high activation energy.

Indeed, at the testing temperatures, the Cu-rich phase is the softest phase among the other phases. In the forged material, it is present in the form of layers between the particles of other phases, and therefore, it is reasonable to assume that the plastic deformation at early stages is localized inside the Cu-rich phase, facilitating sliding of neighbor phase particles. Unfortunately, not all interface boundaries are covered with the Cu-rich phase and the continuous deformation creates constraints between the phases, resulting in an increase in strength. Spheroidization of the Cu-rich phase layers additionally promotes deformation incompatibility between neighbor phase particles. Eventually, other phases start to deform triggering phase transformations inside individual particles and result in a decrease in the plastic flow stress (the softening stage). As soon as the phase transformations are complete, the steady-state flow stage occurs at which GBS is accommodated by the plastic deformation inside the equilibrium high-temperature phases. The stress exponent n at this stage is $n = 2.7$. This value is between $n = 2$, typical to GBS, and $n = 3$, typical to dislocation glide controlled by complex interactions with solute atmospheres.^{27,47} In highly alloyed materials, the latter process often requires increased activation energy.⁴⁷

The fact that the activation energy of the superplastic flow of the AlCoCrCuFeNi HEA indeed approaches a high value of $Q_{ss} = 394 \text{ kJ/mol}$ when the steady-state flow stage is achieved may confirm that the rate-controlling mechanism of the superplastic deformation at this stage is based on the solute-dislocation interactions.

SUMMARY AND CONCLUSIONS

1. The coarse dendritic structure of the as-cast AlCoCrCuFeNi HEA consists of four phases. These are (i) Cu-rich phase with an ordered fcc structure, (ii) Al-Ni-rich phase with an ordered B2 structure, (iii) Cr-Fe-rich phase with a disordered bcc structure, and (iv) Co-Cr-Fe-rich phase with an ordered fcc structure.
2. Multidirectional, isothermal hot forging transformed the dendritic structure into a fine multiphase equiaxed structure with the average grain/particle size of $\sim 2.1 \mu\text{m}$. The hot forging destroyed ordering of the Cu-rich and Co-Cr-Fe-rich phases and transformed the bcc Cr-Fe-rich phase to a tetragonal σ phase.
3. The phases had distinctively different room-temperature nanohardness and elastic modulus in both as-cast and hot-forged conditions. The Cu-rich phase had the lowest nanohardness of 3.8 GPa and 3.0 GPa in as-cast and forged states, respectively. The elastic modulus of the Cu-rich phase was 158 GPa–162 GPa. The remaining Co-Cr-Fe-rich, Al-Ni-rich, and σ phases had nanohardness of 4.1 GPa, 6.8 GPa, and 9.9 GPa, and elastic modulus of 205 GPa, 190 GPa, and 233 GPa, respectively, in hot forged condition.
4. The forged alloy exhibited unusual superplastic behavior during tensile deformation at temperatures of 800°C – 1000°C and at strain rates of 10^{-4} s^{-1} – 10^{-1} s^{-1} . The superplastic behavior was accompanied by a pronounced softening stage, followed by a steady-state flow stage. In spite of the extended softening stage, no noticeable strain localization was observed and the total elongation of up to 1240% was obtained.
5. The dependence of the flow stress σ on strain rate $\dot{\varepsilon}$ and absolute temperature T was described by the relationship $\dot{\varepsilon} = A\sigma^n \exp(-Q/RT)$. The parameters n , Q , and A had unique values at different stages of the plastic deformation. At the beginning of deformation, they had the following values: $n_{0.2} = 1.8$, $Q_{0.2} = 237 \text{ kJ/mol}$, and $A_{0.2} = 5.57 \times 10^5 \text{ s}^{-1} \text{ MPa}^{-n}$. At the strain values corresponding to the peak stress and strain softening stage, these parameters increased to $n_p = 2.0$, $Q_p = 262 \text{ kJ/mol}$, and $A_p = 2.13 \times 10^6 \text{ s}^{-1} \text{ MPa}^{-n}$. When the steady-state flow occurred, n , Q and A reached their maximum values of $n_{ss} = 2.7$, $Q_{ss} = 394 \text{ kJ/mol}$ and $A_{ss} = 7.73 \times 10^{12} \text{ s}^{-1} \text{ MPa}^{-n}$.
6. No noticeable changes in the average grains/particle size occurred after the superplastic

deformation. However, several observations, such as variations in the volume fractions of the phases, changes in the chemical composition of the phases, disappearance of the σ phase, and appearance of a Cr-Fe phase, suggested that the phase transformations occurred during the tensile testing.

7. The analysis of the obtained results suggested that GBS was the main mechanism of the superplastic deformation of the AlCoCrCuFeNi alloy. The formation of porosity at grain boundaries, which is generally associated with GBS, was prevented or slowed down by diffusion-controlled accommodation processes activated inside the grains of different phases. These accommodation processes were different at different stages of the superplastic deformation. It was proposed that GBS was accommodated by (i) the thermally activated deformation of a soft Cu-rich phase at the beginning of the plastic deformation, (ii) the transformations of the low-temperature phases into equilibrium high-temperature phases during the strain-softening stage, and (iii) dislocation glide in the equilibrium high-temperature phases, which was controlled by complex solute-dislocation interactions during a steady-state flow stage.

ACKNOWLEDGEMENT

The financial support from the Ministry of Science and Education of Russian Federation through the Grant No. 02.11.740.5184 is kindly appreciated.

REFERENCES

1. J.-W. Yeh, S.-K. Chen, S.-J. Lin, J.-Y. Gan, T.-S. Chin, T.T. Chun, C.H. Tsau, and S.-Y. Chang, *Adv. Eng. Mater.* 6, 299 (2004).
2. J.-W. Yeh, *Ann. Chim. Sci. Mater.* 31, 633 (2006).
3. J.-W. Yeh, Y.-L. Chen, S.-J. Lin, and S.-K. Chen, *Mater. Sci. Forum* 560, 1 (2007).
4. Y.J. Zhou, Y. Zhang, Y.L. Wang, and G.L. Chen, *Mater. Sci. Eng. A* 454–455, 260 (2007).
5. Y.J. Zhou, Y. Zhang, Y.L. Wang, and G.L. Chen, *Appl. Phys. Lett.* 90, 180904 (2007).
6. Y.J. Zhou, Y. Zhang, F.J. Wang, Y.L. Wang, and G.I. Chen, *J. Alloys Compd.* 466, 201 (2008).
7. Y.P. Wang, B.S. Li, M.X. Ren, C. Yang, and H.Z. Fu, *Mater. Sci. Eng. A* 491, 154 (2008).
8. F.J. Wang and Y. Zhang, *Mater. Sci. Eng. A* 496, 214 (2008).
9. L.H. Wen, H.C. Kou, J.S. Li, H. Chang, X.Y. Xue, and L. Zhou, *Intermetallics* 17, 266 (2009).
10. C.W. Tsai, M.H. Tsai, J.W. Yeh, and C.C. Yang, *J. Alloys Compd.* 490, 160 (2010).
11. J.M. Zhu, H.M. Fu, H.F. Zhang, A.M. Wang, H. Li, and Z.H. Hu, *Mater. Sci. Eng. A* 527, 6975 (2010).
12. O.N. Senkov, G.B. Wilks, J.M. Scott, and D.B. Miracle, *Intermetallics* 19, 698 (2011).
13. O.N. Senkov, J.M. Scott, S.V. Senkova, D.B. Miracle, and C.F. Woodward, *J. Alloys Compd.* 509, 6043 (2011).
14. S. Singh, N. Wanderka, B.S. Murty, U. Glatzel, and J. Banhart, *Acta Mater.* 50, 182 (2011).
15. T.T. Shun, C.-H. Hung, and C.-F. Lee, *J. Alloys Compd.* 493, 105 (2010).
16. Y.P. Wang, B.S. Li, and H.Z. Fu, *Adv. Eng. Mater.* 11, 641 (2009).
17. C.-W. Tsai, Y.-L. Chen, M.-H. Tsai, J.-W. Yeh, T.-T. Shun, and S.K. Chen, *J. Alloys Compd.* 486, 427 (2009).

18. O.N. Senkov, G.B. Wilks, D.B. Miracle, C.P. Chuang, and P.K. Liaw, *Intermetallics* 18, 1758 (2010).
19. A.V. Kuznetsov, D.G. Shaysultanov, N.D. Stepanov, G.A. Salishchev, and O.N. Senkov, *Mater. Sci. Eng. A* 533, 107 (2012).
20. A.V. Kuznetsov, D.G. Shaysultanov, N.D. Stepanov, G.A. Salishchev, and O.N. Senkov, *Mater. Sci. Forum* 735, 146 (2013).
21. A.M. Soifer, A. Verdyan, M. Kazakevich, and E. Rabkin, *Scr. Mater.* 47, 799 (2004).
22. T. Ohmura, K. Tsuzaki, K. Sawada, and K. Kimura, *J. Mater. Res.* 21, 1229 (2003).
23. G.E. Dieter, *Mechanical Metallurgy*, 3rd ed. (New York, NY: McGraw-Hill, Inc., 1986).
24. H.J. McQueen and J.J. Jonas, *Treatise on Materials Science and Technology*, vol. 6, ed. R.J. Arsenault (New York, NY: Academic Press, 1975), pp. 393–493.
25. J.J. Jonas, C.M. Sellars, and W.J. Mc.G. Tegart, *Met Rev.* 14, 1 (1969).
26. G. Effenberg, *Landolt-Bornstein. Numerical Data and Functional Relationships in Science and Technology. New Series IV/11A2* (Stuttgart: MSIT Material Science International Team, 2005), pp. 104–126.
27. T.G. Nieh, J. Wadsworth, and O.D. Sherby, *Superplasticity in Metals and Ceramics Cambridge Solid State Science Series* (Cambridge, MA: Cambridge University Press, 1997).
28. C.M. Lin and H.L. Tsai, *Mater. Chem. Phys.* 128, 50 (2011).
29. Ch.-Ch. Hsieh and W. Wu, *ISRN Metallurgy Article ID* 732491 (2012).
30. Z. Liu, S. Guo, X. Liu, J. Ye, Y. Yang, X.-L. Wang, L. Yang, K. An, and C.T. Liu, *Scr. Mater.* 64, 868 (2011).
31. G. Effenberg, *Landolt-Bornstein. Numerical Data and Functional Relationships in Science and Technology. New Series IV/11D2* (Stuttgart: MSIT Material Science International Team, 2005), pp. 1–36.
32. The Stainless Steel information Center, *High Temperature Properties*, <http://www.ssina.com/composition/temperature.html>. Accessed 17 Aug 2013.
33. R. Darolia, *JOM* 43, 44 (1991).
34. O.A. Kaibyshev, *Superplasticity of Alloys, Intermetallides and Ceramics* (Berlin: Springer, 1992).
35. R.M. Imayev, O.A. Kaibyshev, and G.A. Salishchev, *Acta Metall.* 40, 581 (1992).
36. K.Y. Tsai, M.H. Tsai, and J.W. Yeh, *Acta Mater.* 61, 4887 (2013).
37. C. Ng, S. Guo, J. Luan, S. Shi, and C.T. Liu, *Intermetallics* 31, 165 (2012).
38. C. Zhang, F. Zhang, S. Chen, and W. Cao, *JOM* 64, 839 (2012).
39. D.B. Butrymowicz, J.R. Manning, and M.E. Read, *J. Phys. Chem. Ref. Data* 2, 643 (1973).
40. M. Sakamoto, *J. Phys. Soc. Jpn.* 13, 845 (1958).
41. A.A. Vasilyev, S.F. Sokolov, N.G. Kolbasnikov, and D.F. Sokolov, *Phys. Solid State* 53, 2194 (2011).
42. H.J. Frost and M.F. Ashby, *Fundamental Aspects of Structural Alloy Design* (New York, NY: Plenum Press, 1977).
43. S. Meagher, R.S. Borch, J. Groza, A.K. Mukherjee, and H.W. Green II, *Acta Metall. Mater.* 40, 159 (1992).
44. A. Chaudhuri, *Met. Sci.* 3, 159 (1969).
45. J.L. Campbell and C.W. Schulte, *J. Appl. Phys.* 19, 149 (1979).
46. W. Ren, J. Guo, G. Li, and J. Wu, *Mater. Trans.* 42, 1731 (2004).
47. M.E. Kassner and M.T. Pérez-Prado, *Fundamentals of Creep in Metals and Alloys* (Amsterdam: Elsevier, 2004).